Journal of Solid State Chemistry **162,** 10–19 (2001)
doi:10.1006/jssc.2001.9335, available online at http://www.idealibrary.com on IDEAL®

# *Ab Initio* Determination of $Bi_{4.86}La_{1.14}O_9$ Monoclinic Structure from Powder Neutron Diffraction Data. Characterization of the Related Solid Solution

S. Obbade, M. Drache,[1] and P. Conflant

*Laboratoire de Cristallochimie et Physicochimie du Solide, UPRESA 8012 CNRS, USTL-ENSCL, BP 108, 59652 Villeneuve d'Ascq Cedex, France*

and

E. Suard

*ILL, Avenue des Martyrs, BP 156, 38042 Grenoble Cedex 9, France*

Received April 25, 2001; in revised form July 17, 2001; accepted August 1, 2001

**This paper deals with the *ab initio* determination of ε-$Bi_{4.86}La_{1.14}O_9$ monoclinic structure from powder neutron data using the Rietveld method, and with physical properties characterization of a related solid solution. ε-$Bi_{4.86}La_{1.14}O_9$, obtained from the annealing of a quenched rhombohedral high-temperature $\beta_1$ sample, is monoclinic, $P2/c$, $a = 9.4956(3)$ Å, $b = 3.9742(1)$ Å, $c = 7.0425(2)$ Å, $\beta = 104.700(2)^\circ$; $Z = 1$. The structure refinement converged to $R_F = 0.043$ and $R_{Bragg} = 0.047$. The structure is built from cationic slabs parallel to (100) faces of the monoclinic cell. Each cell corresponds to one slab containing a mixed $Bi_{0.86}La_{1.14}$ cationic layer ($Bi_{(1)}$) sandwiched between two equivalent bismuth layers ($Bi_{(2)}$). The cohesion of the cations in the slabs results from the presence of the oxygen atoms distributed over three sites. Six $O_{(1)}$ and two $O_{(2)}$ atoms form a slightly distorted cubical polyhedron around the mixed cationic site ($Bi_{(1)}$). $Bi_{(2)}$ atoms are surrounded by seven oxygen atoms in a very distorted polyhedron. The important delocalization of $Bi_{(2)}$ lone pairs toward the interslab spaces leads to significant bonds with the adjacent slabs and to the cohesion of the structure. ε-$Bi_{4.86}La_{1.14}O_9$ is the low symmetry variety of a particular sample of a wide solid solution domain that, formulated $Bi_{1-x}La_xO_{1.5}$, has been investigated for $0.15 \leq x \leq 0.325$. The formation of this phase from the irreversible transformation of quenched-$\beta_1$ on heating and the subsequent transitions $\varepsilon \rightarrow \beta_2 \rightarrow \beta_1$ have been evidenced by thermodiffractometry, conductivity measurements versus temperature, dilatometry, and thermal analyses. Thermal expansion coefficients ($\times 10^5$) are for *a*, *c*, and/or lattice volume for a quenched-$\beta_1$, ε, $\beta_2$, or $\beta_1$ variety of $Bi_{4.86}La_{1.14}O_9$ ($x = 0.19$) respectively: 1.74, − 0.72, 2.78; 5.25; 1.74, 1.81, 5.37; 0.99, 1.08, 3.90. The corresponding activation energies are 0.94, 0.83, 0.84, and 0.21 eV. The $\varepsilon \rightarrow \beta_2$ transition, irreversible for $0.15 \leq x \leq 0.275$, appears partly reversible for $0.3 \leq x \leq 0.325$.** © 2001 Academic Press

***Key Words:*** **rhombohedral Bi–Sr–O-type materials; *ab initio* crystal structure determination; bismuth lanthanum-based mixed oxides; electronic lone pair; oxide conductors; Rietveld structure refinement; neutron diffraction.**

## INTRODUCTION

A recent investigation of structural and conductivity properties of $Bi_{0.775}Ln_{0.225}O_{1.5}$ oxide conductors ($Ln$ = La, Pr, Nd, Sm, Eu, Gd, Tb, Dy), which belong to the dimorphic rhombohedral Bi–Sr–O structural-type family, has proved a close conductivity–composition dependence (1). This has been interpreted on the basis of structural data obtained from Rietveld structure refinements based on previous crystal structure investigations (2–10). The structure is built from cationic slabs parallel to (001) faces of the hexagonal cells. There are nine formula units $Bi_{0.775}Ln_{0.225}O_{1.5}$ per hexagonal cell, distributed over three slabs. Each slab is constituted from a mixed $Bi^{3+}/Ln^{3+}$ layer, sandwiched between two $Bi^{3+}$ layers, and two oxygen sites are located inside; complementary oxide ions, implied by the formulation stoichiometries, are distributed over one or two sites of the interslab space and exhibit a high mobility, mainly responsible for the conductivity (4, 6).

Depending on the rare-earth nature, a $\beta_1$ high-temperature form is observed, with a closely hexagonal related structure; its formation from the $\beta_2$ low-temperature variety occurs during a phase transition that has been attributed to a cationic disordering in the mixed $Bi^{3+}/Ln^{3+}$ layers. It is accompanied by sudden increases of both lattice

[1] To whom correspondence should be addressed. Fax: (33)320436814. E-mail: drache@ensc-lille.fr.



0022-4596/01 $35.00

parameters, of oxide occupancy in interslab spaces, and of the conductivity. The pure ion oxide conductor character of the $\beta_1$ variety has been clearly demonstrated for the alkaline-earth-based solid solutions (4), and has been also verified for lanthanides-based solid solutions (unpublished results).

The thickness of the cationic slabs, which is the largest for the lanthanum term $Bi_{0.775}La_{0.225}O_{1.5}$ (the best oxide conductor ever evidenced in this family: $\sigma_{400°C} = 10^{-3}$ S cm$^{-1}$ with $E_a = 0.8$ eV), appears to be an important factor for these attractive conductivity properties.

$Bi_{0.775}La_{0.225}O_{1.5}$ is a term of a wide $Bi_{1-x}La_xO_{1.5}$ solid solution domain, with $0.15 \leq x \leq 0.333$, which exhibits anomalies in the evolution of the cell parameters versus composition (14); for one of the particular compositions "$Bi_{17}La_4O_{31.5}$," which is identical to $Bi_{4.86}La_{1.14}O_9$ or $Bi_{0.81}La_{0.19}O_{1.5}$ ($x = 0.19$), a thermal investigation of the quenched $\beta_1$ high-temperature form led to evidence of a new monoclinic variety $\varepsilon$ (15). This paper deals with the *ab initio* structure determination of this new phase from powder neutron diffraction data; identification and investigation of the corresponding solid solution, using various techniques such as X-ray diffractometry (at ambient pressure and versus the temperature), dilatometry, impedance spectrometry, and thermal analyses (DTA), are also presented.

## EXPERIMENTAL

### *Syntheses*

Bismuth–lanthanum-based oxide powder samples were prepared by solid state reaction of mixtures of $Bi_2O_3$ and $La_2O_3$. The reactants were prefired in air overnight at 600 and 700°C respectively, in order to prevent any trace of hydrate or carbonate; then stoichiometric proportions corresponding to the formula $Bi_{1-x}La_xO_{1.5}$ ($0.15 \leq x \leq 0.325$) were accurately weighed and thoroughly ground in an agate mortar. Mixtures were heated in open alumina crucibles for several 15-h treatments and air-quenched; each thermal treatment was followed by a regrinding. Heating temperatures and the number of thermal treatments were determined previously (14). Final sample quenching in air or in liquid nitrogen was realized from 800°C, for all compositions investigated.

A pure $\beta$-rhombohedral Bi–Sr–O-type phase, characterized by Guinier de Wolff patterns, was obtained within a composition range depending on the quenching conditions, whereas the adjacent domain for higher lanthanum content was relative to a mixture of rhombohedral- and $\varepsilon$-$Bi_{0.81}La_{0.19}O_{1.5}$-type phases. The limits of the domains are $0.15 \leq x \leq 0.20$ and $0.225 \leq x \leq 0.325$ for samples quenched in ambient air, or $0.15 \leq x \leq 0.275$ and $0.30 \leq x \leq 0.325$ when the quenching medium was liquid nitrogen.

For each composition examined, a fraction of the sample initially quenched in liquid nitrogen was subsequently annealed at 300°C for 2 to 3 days, taking into account the synthesis process of the $\varepsilon$-$Bi_{0.81}La_{0.19}O_{1.5}$ monoclinic form as previously described (15).

### *Physical Measurements*

X-ray powder diffraction data were obtained on a Siemens D5000 diffractometer using a Bragg Brentano geometry, with a back-monochromatized Cu$K\alpha$ radiation. Diffraction spectra were scanned by steps of 0.02° ($2\theta$) over the angle range 15–100°, with a counting time of 1.5 s per step. Each sample was rotated 3.14 rad s$^{-1}$ during the data recording, in order to minimize the orientation effects resulting from the material compaction. The pattern peak positions are extracted with the Topas P of Bruker-Diffrac$^{plus}$ software package, where each peak profile is refined using the pseudo-Voigt function. The accurate cell parameters of the different samples were refined from 20 to 30 reflections (hexagonal or monoclinic setting).

The crystal structure determination of the $\varepsilon$ phase was carried out for the $Bi_{0.81}La_{0.19}O_{1.5}$ parent composition. The first attempts were undertaken by recording X-ray diffraction data, but each time, the intensities diffraction pattern was erroneous by the preferential orientation phenomenon.

To minimize the preferential orientation effect and indeed be able to separate the oxygen atoms of the heavy atoms Bi and La, room temperature neutron powder diffraction data were collected using the high-resolution D1A diffractometer at the Institute Laue Langevin (ILL) neutron source, in Grenoble. The pattern of the compound was scanned over the angular range 10° to 160° with increments of $\Delta(2\theta) = 0.05°$, using an incident constant wavelength 1.911 Å selected from the Ge (511) monochromator. A powder sample ($\sim$ 10 g) was enclosed in a cylindrical vanadium container of 9 mm inner diameter, and the pattern was collected over 15 h. The crystal structure determination has been concluded by using alternately the FULLPROF (16) and EXPO (17, 18) programs.

The thermal behavior of the quenched samples was investigated either for few a selected compositions or for an extensive number of samples, depending on the envisaged technique.

X-ray thermodiffractometry studies were carried out using Siemens HTK10 high-temperature device (heating platinum blade; average heating rate 300°C h$^{-1}$; air gas flow). The samples were deposited using an ethanol slurry, which yields upon evaporation a regular layer of powdered compound.

Dilatometric and conductivity investigations were made on samples pelletized at room temperature (diameter 5 mm, thickness approx. 3 mm), then sintered at 900°C for 15 h and quenched to room temperature, in liquid nitrogen. The degree of compactness in all cases ranged between 75 and 92%.

Dilatometric studies were performed on a Linseis L75 dilatometer with a heating rate of 0.4°C/min between 20 and 700°C.

For conductivity measurements, gold electrodes were vacuum deposited on both flat surfaces of the pellets using the sputtering method. The measurements were obtained by impedance spectrometry in the frequency range 1–$10^6$ Hz, using a frequency response analyzer Schlumberger 1170; for a given temperature, each set of values was recorded after a 1-h stabilization time.

Thermal analyses were conducted on Setaram D.T.A. 92-1600 apparatus, between 20 and 850°C with a heating or cooling rate 300° $h^{-1}$, using platinum or gold crucibles.

## RESULTS AND DISCUSSION

### *Quenched-$\beta_1$ Form Identification*

The recent study of the $Bi_{0.81}La_{0.19}O_{1.5}$ sample, for which the monoclinic ε phase was evidenced (15), has shown that the preparation of a pure quenched form of $\beta_1$ is the first necessary step for the monoclinic ε preparation.

The X-ray diffraction diagrams of samples quenched in liquid nitrogen from 800°C have been indexed with the reflections setting of the $\beta_1/\beta_2$-type hexagonal cell. Figure 1 reports the refined cell parameters evolution versus composition with the lattice constants obtained previously for the samples annealed at 620°C (14). The discernment of both series of samples can be realized for two composition ranges: For $x > 0.275$, it can result evidently from the two-phased state of the quenched samples, whereas the annealed samples are single phased. In the composition range $0.166 < x < 0.2$, a limited region of the domains of pure hexagonal phases, the cell parameters of the annealed phase exhibit the regular evolution previously described, whereas the lattice constants of quenched samples reveal breaking points for $x = 0.166$, 0.190, and 0.2; the evolution graphs are particularly distinguished for $x = 0.190$. It appears more evident to verify, for the corresponding sample $Bi_{0.81}La_{0.19}O_{15}$, the purity of the quenched $\beta_1$ form and to assure the final purity of ε after the subsequent annealing treatment. This led us to retain this composition for the Rietveld structure determination, which has been realized.

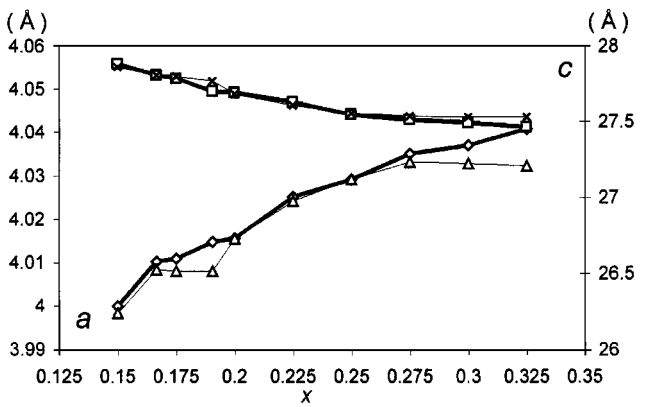


**FIG. 1.** Composition dependence of cell parameters for $Bi_{1-x}La_xO_{1.5}$ rhombohedral phases quenched in liquid nitrogen from 800°C ($\beta_1$ domain: △, *x*) or from 600°C ($\beta_2$ domain: ◇, □).

**TABLE 1**
**Crystal and Refinement Parameters for $Bi_{4.86}La_{1.14}O_9$**

| | |
|---|---|
| Formula weight | 1318 |
| Crystal system | Monoclinic |
| Space group | *P*2/*c* |
| Unit cell dimensions | |
| *a*, Å | 9.4956(3) |
| *b*, Å | 3.9742(1) |
| *c*, Å | 7.0425(2) |
| β, deg | 104.700(2) |
| *v*, Å$^3$ | 257.04(4) |
| Unit formula | $Z = 1$ |
| Density (calculated), g/cm$^3$ | 8.50 |
| Sample description | Yellow powder |
| No. of reflections | 292 |
| No. of fitted parameters | 48 |
| No. of profile points | 3350 |
| Profiles function | pseudo-Voigt |
| | $\eta = 0.22(3)$ |
| Half-width parameters | |
| *U* | 0.25(1) |
| *V* | −0.43(2) |
| *W* | 0.35(1) |
| *R* factors | |
| $R_{exp}$ | 0.048 |
| $R_p$ | 0.045 |
| $R_{wp}$ | 0.058 |
| $R_F$ | 0.043 |
| $R_B$ | 0.047 |
| $\chi^2$ | 1.42 |

### *Monoclinic ε-$Bi_{4.86}La_{1.14}O_9$ Structure*

*Structure determination.* In the X-ray diffraction study (Cu*K*α radiation) of the $Bi_{0.81}La_{0.19}O_{1.5}$ sample (15),

**TABLE 2**
**Final Refined Atomic Positions, Occupancy, and Equivalent Isotropic Thermal Displacement Factors for $Bi_{4.86}La_{1.14}O_9$**

| Atoms | Sites | *x* | *y* | *z* | $B_{eq}$ (Å$^2$)[a] | Occup. |
|---|---|---|---|---|---|---|
| $La/Bi_{(1)}$ | 2f | 0.5 | 0.2555(16) | 0.25 | 2.31(2) | 1.14/0.86 |
| $Bi_{(2)}$ | 4g | 0.8283(2) | 0.2624(12) | 0.0304(4) | 1.95(2) | 4 |
| $O_{(1)}$ | 4g | 0.3994(4) | 0.7596(16) | 0.0488(6) | 2.51(4) | 4 |
| $O_{(2)}$ | 4g | 0.2205(5) | 0.7903(30) | 0.6656(10) | 4.58(4) | 2.87(3) |
| $O_{(3)}$ | 4g | 0.1835(16) | 0.1792(24) | 0.8235(20) | 11.71(9) | 2.13(3) |

[a] $B_{eq} = \frac{4}{3} \sum_i \sum_j \beta_{ij} a_i a_j$.

**TABLE 3**
**Anisotropic Thermal Displacement Factors $\beta_{ij}$[a] for $Bi_{4.86}La_{1.14}O_9$**

| Atoms | $\beta_{11}$ | $\beta_{22}$ | $\beta_{33}$ | $\beta_{12}$ | $\beta_{13}$ | $\beta_{23}$ |
|---|---|---|---|---|---|---|
| $Bi_{(1)}$, La | 0.0130(5) | 0.0272(33) | 0.0046(10) | 0 | 0.0031(6) | 0 |
| $Bi_{(2)}$ | 0.0042(3) | 0.0324(23) | 0.0109(7) | 0.0015(14) | − 0.0006(4) | − 0.0137(15) |
| $O_{(1)}$ | 0.0028(4) | 0.0284(32) | 0.0243(11) | 0.0195(19) | − 0.0005(6) | 0.0103(26) |
| $O_{(2)}$ | 0.0105(9) | 0.0937(71) | 0.0262(19) | 0.0029(26) | 0.0087(13) | 0.0008(44) |
| $O_{(3)}$ | 0.0522(35) | 0.0269(98) | 0.0525(42) | − 0.0456(49) | − 0.0281(29) | 0.0435(54) |

[a] The anisotropic displacement exponent takes the form $-(\beta_{11}h^2 + \beta_{22}k^2 + \beta_{33}l^2 + \beta_{12}hk + \beta_{13}hl + \beta_{23}kl)$.

**TABLE 4**
**Bond Lengths (Å) and Selected Angles (°) for $Bi_{4.86}La_{1.14}O_9$**

| La–$Bi_{(1)}$ environment | | $Bi_{(2)}$ environment | |
|---|---|---|---|
| $Bi_{(1)}$–$O_{(1)}$ | 2.50(1) | $Bi_{(2)}$–$O^{(iv)}_{(1)(1\,1\,0)}$ | 2.09(1) |
| $Bi_{(1)}$–$O^{(i)}_{(1)(0\,\bar1\,0)}$ | 2.47(1) | $Bi_{(2)}$–$O^{(ii)}_{(2)(1\,\bar1\,0)}$ | 2.31(2) |
| $Bi_{(1)}$–$O^{(ii)}_{(1)(1\,\bar1\,0)}$ | 2.47(1) | $Bi_{(2)}$–$O^{(ii)}_{(2)(1\,0\,0)}$ | 2.49(2) |
| $Bi_{(1)}$–$O^{(ii)}_{(2)(1\,0\,0)}$ | 2.50(1) | $Bi_{(2)}$–$O^{(iv)}_{(2)(1\,1\,1)}$ | 2.31(1) |
| $Bi_{(1)}$–$O^{(iii)}_{(1)(0\,1\,0)}$ | 2.52(1) | $Bi_{(2)}$–$O^{(ii)}_{(3)(1\,0\,0)}$ | 2.49(2) |
| $Bi_{(1)}$–$O^{(iv)}_{(1)(1\,1\,0)}$ | 2.52(1) | $Bi_{(2)}$–$O^{(iv)}_{(3)(1\,0\,1)}$ | 2.05(1) |
| $Bi_{(1)}$–$O^{(iii)}_{(2)(0\,1\,\bar1)}$ | 2.57(1) | $Bi_{(2)}$–$O^{(iv)}_{(3)(1\,1\,1)}$ | 2.46(2) |
| $Bi_{(1)}$–$O^{(iv)}_{(2)(1\,1\,1)}$ | 2.57(1) | | |
| mean | 2.51(1) | mean | 2.31(1) |
| Selected angles | | | |
| $O_{(1)}$–$Bi_{(1)}$–$O^{(i)}_{(1)(0\,\bar1\,0)}$ | 106.1(4) | $O^{(iv)}_{(1)(1\,1\,0)}$–$Bi_{(2)}$–$O^{(ii)}_{(2)(1\,\bar1\,0)}$ | 76.7(4) |
| $O_{(1)}$–$Bi_{(1)}$–$O^{(ii)}_{(1)(1\,\bar1\,0)}$ | 179.5(4) | $O^{(iv)}_{(1)(1\,1\,0)}$–$Bi_{(2)}$–$O^{(ii)}_{(2)(1\,0\,0)}$ | 81.6(5) |
| $O_{(1)}$–$Bi_{(1)}$–$O^{(ii)}_{(1)(1\,0\,0)}$ | 73.4(3) | $O^{(iv)}_{(1)(1\,1\,0)}$–$Bi_{(2)}$–$O^{(iv)}_{(2)(1\,1\,1)}$ | 78.9(3) |
| $O_{(1)}$–$Bi_{(1)}$–$O^{(iii)}_{(1)(0\,1\,0)}$ | 108.7(3) | $O^{(iv)}_{(1)(1\,1\,0)}$–$Bi_{(2)}$–$O^{(ii)}_{(3)(1\,0\,0)}$ | 86.9(7) |
| $O_{(1)}$–$Bi_{(1)}$–$O^{(iv)}_{(1)(1\,1\,0)}$ | 73.6(2) | $O^{(iv)}_{(1)(1\,1\,0)}$–$Bi_{(2)}$–$O^{(iv)}_{(3)(1\,0\,1)}$ | 85.1(6) |
| $O_{(1)}$–$Bi_{(1)}$–$O^{(iii)}_{(2)(0\,1\,\bar1)}$ | 72.7(4) | $O^{(iv)}_{(1)(1\,1\,0)}$–$Bi_{(2)}$–$O^{(iv)}_{(3)(1\,1\,1)}$ | 89.7(6) |
| $O_{(1)}$–$Bi_{(1)}$–$O^{(iv)}_{(2)(1\,1\,1)}$ | 114.3(4) | $O^{(ii)}_{(2)(1\,\bar1\,0)}$–$Bi_{(2)}$–$O^{(ii)}_{(2)(1\,0\,0)}$ | 111.9(8) |
| $O^{(i)}_{(1)(0\,1\,0)}$–$Bi_{(1)}$–$O^{(ii)}_{(1)(1\,\bar1\,0)}$ | 74.3(3) | $O^{(ii)}_{(2)(1\,\bar1\,0)}$–$Bi_{(2)}$–$O^{(iv)}_{(2)(1\,1\,1)}$ | 115.1(6) |
| $O^{(i)}_{(1)(0\,1\,0)}$–$Bi_{(1)}$–$O^{(ii)}_{(1)(1\,0\,0)}$ | 179.3(3) | $O^{(ii)}_{(2)(1\,\bar1\,0)}$–$Bi_{(2)}$–$O^{(ii)}_{(3)(1\,0\,0)}$ | 48.8(5) |
| $O^{(i)}_{(1)(0\,1\,0)}$–$Bi_{(1)}$–$O^{(iii)}_{(1)(0\,1\,0)}$ | 106.6(3) | $O^{(ii)}_{(2)(1\,\bar1\,0)}$–$Bi_{(2)}$–$O^{(iv)}_{(3)(1\,0\,1)}$ | 64.9(6) |
| $O^{(i)}_{(1)(0\,1\,0)}$–$Bi_{(1)}$–$O^{(iv)}_{(1)(1\,1\,0)}$ | 71.1(3) | $O^{(ii)}_{(2)(1\,\bar1\,0)}$–$Bi_{(2)}$–$O^{(iv)}_{(3)(1\,1\,1)}$ | 163.9(8) |
| $O^{(i)}_{(1)(0\,1\,0)}$–$Bi_{(1)}$–$O^{(iii)}_{(2)(0\,1\,\bar1)}$ | 65.5(3) | $O^{(ii)}_{(2)(1\,0\,0)}$–$Bi_{(2)}$–$O^{(iv)}_{(2)(1\,1\,1)}$ | 122.5(6) |
| $O^{(i)}_{(1)(0\,1\,0)}$–$Bi_{(1)}$–$O^{(iv)}_{(2)(1\,1\,1)}$ | 107.5(4) | $O^{(ii)}_{(2)(1\,0\,0)}$–$Bi_{(2)}$–$O^{(ii)}_{(3)(1\,0\,0)}$ | 625(6) |
| $O^{(ii)}_{(1)(1\,\bar1\,0)}$–$Bi_{(1)}$–$O^{(ii)}_{(1)(1\,0\,0)}$ | 106.1(4) | $O^{(ii)}_{(2)(1\,0\,0)}$–$Bi_{(2)}$–$O^{(iv)}_{(3)(1\,0\,1)}$ | 166.6(9) |
| $O^{(ii)}_{(1)(1\,\bar1\,0)}$–$Bi_{(1)}$–$O^{(iii)}_{(1)(0\,1\,0)}$ | 71.1(3) | $O^{(ii)}_{(2)(1\,0\,0)}$–$Bi_{(2)}$–$O^{(iv)}_{(3)(1\,1\,1)}$ | 65.6(5) |
| $O^{(ii)}_{(1)(1\,\bar1\,0)}$–$Bi_{(1)}$–$O^{(iv)}_{(1)(1\,1\,0)}$ | 106.6(3) | $O^{(iv)}_{(2)(1\,1\,1)}$–$Bi_{(2)}$–$O^{(ii)}_{(3)(1\,0\,0)}$ | 161.2(8) |
| $O^{(ii)}_{(1)(1\,\bar1\,0)}$–$Bi_{(1)}$–$O^{(iii)}_{(2)(0\,1\,\bar1)}$ | 107.5(4) | $O^{(iv)}_{(2)(1\,1\,1)}$–$Bi_{(2)}$–$O^{(iv)}_{(3)(1\,0\,1)}$ | 53.8(5) |
| $O^{(ii)}_{(1)(1\,\bar1\,0)}$–$Bi_{(1)}$–$O^{(iv)}_{(2)(1\,1\,1)}$ | 65.5(3) | $O^{(iv)}_{(2)(1\,1\,1)}$–$Bi_{(2)}$–$O^{(iv)}_{(3)(1\,1\,1)}$ | 69.7(5) |
| $O^{(ii)}_{(1)(1\,0\,0)}$–$Bi_{(1)}$–$O^{(iii)}_{(1)(0\,1\,0)}$ | 73.6(3) | $O^{(ii)}_{(3)(1\,0\,0)}$–$Bi_{(2)}$–$O^{(iv)}_{(3)(1\,0\,1)}$ | 113.2(9) |
| $O^{(ii)}_{(1)(1\,0\,0)}$–$Bi_{(1)}$–$O^{(iv)}_{(1)(1\,1\,0)}$ | 108.7(3) | $O^{(ii)}_{(3)(1\,0\,0)}$–$Bi_{(2)}$–$O^{(iv)}_{(3)(1\,1\,1)}$ | 122.9(8) |
| $O^{(ii)}_{(1)(1\,0\,0)}$–$Bi_{(1)}$–$O^{(iii)}_{(2)(0\,1\,\bar1)}$ | 114.3(4) | $O^{(iv)}_{(3)(1\,0\,1)}$–$Bi_{(2)}$–$O^{(iv)}_{(3)(1\,1\,1)}$ | 123.2(7) |
| $O^{(ii)}_{(1)(1\,0\,0)}$–$Bi_{(1)}$–$O^{(iv)}_{(2)(1\,1\,1)}$ | 72.7(4) | | |
| $O^{(iii)}_{(1)(0\,1\,0)}$–$Bi_{(1)}$–$O^{(iv)}_{(1)(1\,1\,0)}$ | 177.3(3) | | |
| $O^{(iii)}_{(1)(0\,1\,0)}$–$Bi_{(1)}$–$O^{(iii)}_{(2)(0\,1\,\bar1)}$ | 66.7(3) | | |
| $O^{(iii)}_{(1)(0\,1\,0)}$–$Bi_{(1)}$–$O^{(iv)}_{(2)(1\,1\,1)}$ | 113.1(3) | | |
| $O^{(iv)}_{(1)(1\,1\,0)}$–$Bi_{(1)}$–$O^{(iii)}_{(2)(0\,1\,\bar1)}$ | 113.1(3) | | |
| $O^{(iv)}_{(1)(1\,1\,0)}$–$Bi_{(1)}$–$O^{(iv)}_{(2)(1\,1\,1)}$ | 66.7(3) | | |
| $O^{(iii)}_{(2)(0\,1\,\bar1)}$–$Bi_{(1)}$–$O^{(iv)}_{(2)(1\,1\,1)}$ | 171.9(4) | | |

*Note.* Symmetry code: (i) $x, y, z$; (ii) $-x, y, \frac{1}{2}-z$; (iii) $x, -y, \frac{1}{2}+z$; and (iv) $-x; -y, -z$.

recorded with the D5000 diffractometer and using the program of indexing TREOR (19), the X-ray diagram of this phase has been indexed in a monoclinic system with the following cell parameters $a_1 = 9.492$ Å, $b_1 = 7.951$ Å, $c_1 = 7.028$ Å, and $\beta_1 = 104.74°$. We have therefore begun the structural resolution in this crystalline cell, but during the refinement of the structure, we have noticed that, for all observed reflections $(hkl)$ one has $k = 2n$, and for each atom in $(x, y, z)$ one observes an identical atom in $(x, y + \frac{1}{2}, z)$, which indicates that the true crystalline cell corresponds to half of the precedent with the new cell parameters $a = a_1$, $b = b_1/2$, $c = c_1$, and $\beta = \beta_1$.

To determine the space group, the values of the individual intensities were extracted from the powder pattern, in the centrosymmetric $P2/m$ space group, using the pattern-matching option of the FULLPROF program, where only a cell-constrained whole pattern-fitting program was used. The analysis of the reflections extracted from the powder pattern showed the systematic restrictions $(h0l,\ h + l = 2n)$ that were consistent with $Pc$ and $P2/c$ space groups.

The partial model of the crystal structure has been carried out with the EXPO program (17), in the centrosymmetric space group $P2/c$. This first model was used in the FULLPROF program (16), and several difference Fourier syntheses showed the rest of the structure, which was refined by the Rietveld method (20, 21). A pseudo-Voigt function was chosen to generate the lineshape of the diffraction peaks with an asymmetry correction at low angles. The dependence between the full-width at half maximum (FWHM) and the angle was represented by the function $(\mathrm{FWHM})^2 = U\tan^2\theta + V\tan\theta + W$ (22), where $U$, $V$, and $W$ were parameters refined in the process. The coherent scattering lengths used were Bi = 0.8532, La = 0.8240, and O = 0.5803 fm. The background was defined by a fifth-order polynomial in $2\theta$ and was refined simultaneously with the other profile parameters. Cell dimensions and structural parameters were refined, with independent refinement of the profile parameters, i.e., peak shapes, background parameters, zero point correction, and scale factors.

Taking into account the small difference between the coherent scattering lengths of Bi and La atoms, their

occupancy factors have been fixed to fit the chemical formula. Similarly after the first refinement, it appeared clearly an occupancy factor of oxygen atom $O_{(1)}$ very near to unity, while the two other oxygen sites are partially occupied. Then for the continuation of the refinement, we have fixed the occupancy of $O_{(1)}$ at unity and refined the two other oxygen sites $O_{(2)}$ and $O_{(3)}$ under a linear constraint to respect the chemical formula. In the final refinement, anisotropic thermal parameters were refined for all atoms. Crystal and refinement parameters are summarized in Table 1. The final refined atomic positions, occupancy, and equivalent isotropic thermal displacement factors are shown in Table 2, anisotropic thermal displacement factors for all atoms in Table 3, and selected bond lengths and angles in Table 4. The corresponding fitted diffraction diagrams are shown in Fig. 2.

*Lone-pair electrons localization.* In solid state materials, the phenomenon of the lone-pair electrons is characteristic of heavy metal cations with an external electronic configuration $ns^2np^0$, such as $Bi^{3+}$ and $Pb^{2+}$. Thus, it has been shown that the steric occupation of lone pairs is comparable to the occupation of an anion $O^{2-}$ or $F^-$. Resulting from its weak electronic density, its localization by diffraction is difficult.

In crystalline structures, the lone pair localization is based on the knowledge of the electronic polarizability of its $ns^2np^0$ atom of origin. The delocalization of the lone pair is assumed to be due to the deformation of the electronic cloud of this atom because of that polarization, induced by the existence of the local electric field in the crystal. Thus, the method of the lone-pair location is based on the finding of the equilibrium state between the local electric field and the electronic polarization on an ion. Therefore, the relation between the distance vector to the nucleus of the atom supporting the lone pair ($d$) and the local electric field ($E$) is then ($P = -2d = \alpha E$), where $-2$ is the charge of lone pair and ($\alpha$) the electronic polarizability of the ion, proposed by Shannon (23).

The lone-pair electrons localization was carried out with the program HYBRIDE (24) based on the algorithm of Verbaere *et al.* (25), in which $E$ is calculated by the Ewald method (26), where the polarizability for $Bi^{3+}$ was chosen as $\alpha = 3.0$ Å$^3$. The calculation used to determine ions partial charges derives from the Pauling empirical formula (27), which gives the ionicity rate of an $M$–O bond according to the difference between the electronegativities $\chi_M$ and $\chi_O$ of the $M$ and O atoms. Values of $\chi$ are taken in the electronegativity scale of Allred and Rochow (28). Thus, a percent-

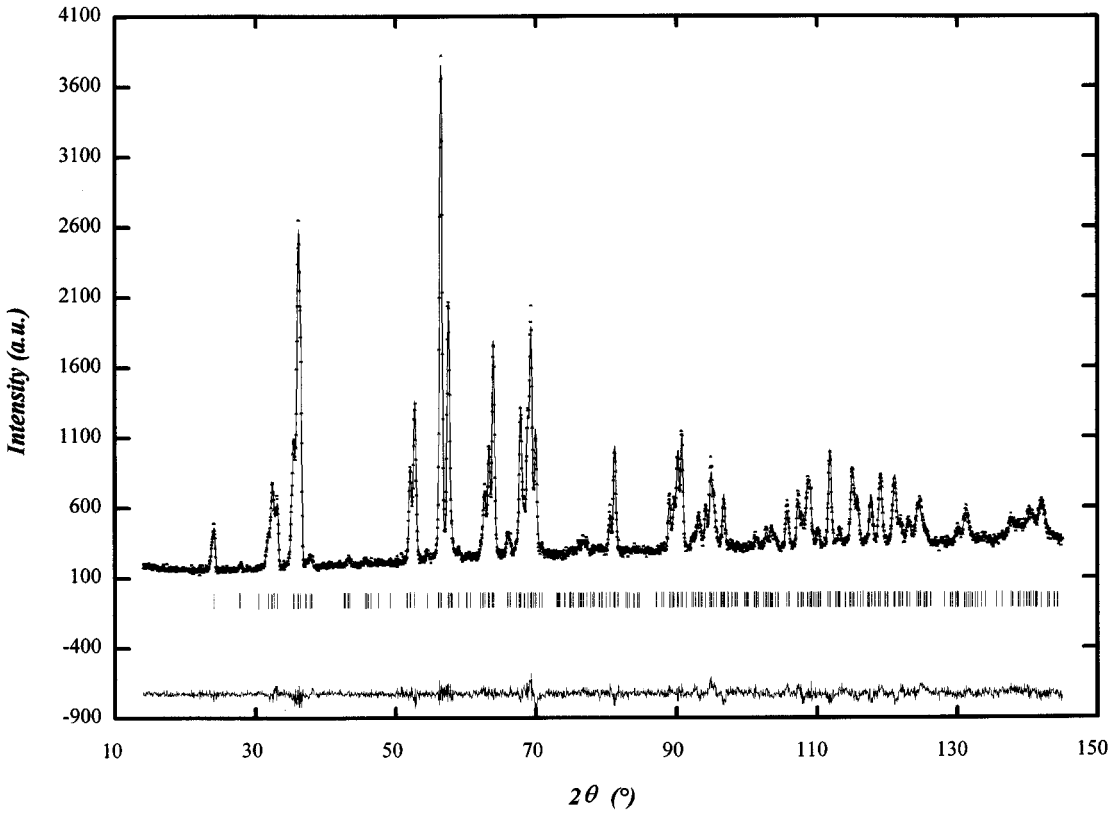


**FIG. 2.** Observed (points) and calculated (continuous line) powder neutron diffraction patterns of $Bi_{4.86}La_{1.14}O_9$; the difference between the observed and calculated patterns appears in the lower part.

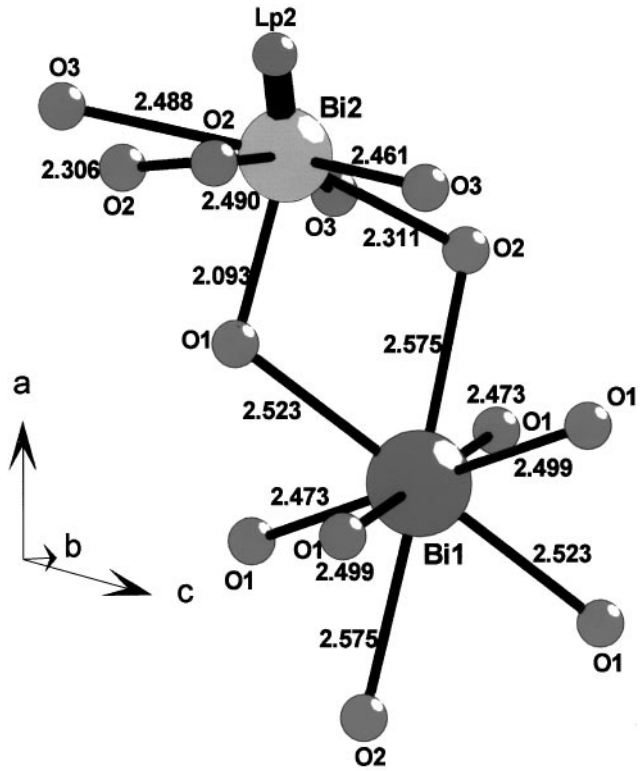


**FIG. 3.** The oxygen environment around cations La–$Bi_{(1)}$ and $Bi_{(2)}$, with the bond lengths (Å).

age formal ionicity value was calculated for each bond using the formula

$$M\text{–O} = 1 - \exp[-(\chi_O - \chi_M)^{2/4}].$$

Calculations for locating bismuth lone pairs require taking into account the substitution rate of the considered atom when it occupies a mixed site, and the occupation rate of oxygen atoms in the partially vacant sites. We have performed the localization of these lone pairs, using the polarizability coefficient $\alpha(Bi^{3+}) = 3.0$ Å.

From atomic positions obtained by neutron diffraction, the location of the $Bi_{(2)}$ lone pair has been determined by using the method described above. Resulting from the largely occupied environment of the $Bi_{(1)}$, La mixed site, not any realistic $Bi_{(1)}$ lone-pair location could be envisaged.

*Crystal structure description.* The crystal structure of this compound can be described by different cationic environments. Each mixed site La–$Bi_{(1)}$ is surrounded by eight oxygen atoms (six $O_{(1)}$ atoms and two $O_{(2)}$ atoms) at normal distances ranging from 2.47 to 2.57 Å with a mean distance $\langle Bi\text{–}O \rangle \cong 2.51$ Å, to form a slightly distorted cubical polyhedron (Fig. 3). This high symmetry of the oxygen environment leads to a very weak stereochemical activity and the nonhybridization of the $Bi_{(1)}$ lone pair (Lp) of the atom, which is likely very close to the bismuth nucleus. The second atom $Bi_{(2)}$ is bonded by seven oxygen atoms to form

**TABLE 5**
**$Bi_{(2)}$ Lone Pair (Lp) Position,[a] Distances (Lp–O), and Angles (Lp–Bi–O) for $Bi_{4.86}La_{1.14}O_9$**

| Lp position | Nucleus–Lp distances (Å) | Lp–O distances (Å) | Lp–Bi–O angles (°) |
|---|---|---|---|
| | $d = 1.22$ | $Lp\text{–}Bi_{(2)} = 1.22$ | |
| | | $Lp\text{–}O_{(3)} = 3.16$ | 143.94 |
| $x = 0.934$ | $dx = 1.10$ | $Lp\text{–}O_{(2)} = 2.77$ | 98.96 |
| $y = 0.366$ | $dy = 0.41$ | $Lp\text{–}O_{(2)} = 3.26$ | 132.34 |
| $z = -0.020$ | $dz = -0.34$ | $Lp\text{–}O_{(3)} = 2.67$ | 86.84 |
| | | $Lp\text{–}O_{(3)} = 2.27$ | 65.43 |
| | | $Lp\text{–}O_{(2)} = 2.30$ | 66.72 |
| | | $Lp\text{–}O_{(2)} = 2.77$ | 39.16 |
| | | $Lp\text{–}O_{(3)} = 2.94$ | 24.69 |
| | | $Lp\text{–}O_{(3)} = 3.43$ | 48.25 |

[a] $d_x$, $d_y$ and $d_z$ are the nucleus–Lp distances projected along $x$, $y$, and $z$.

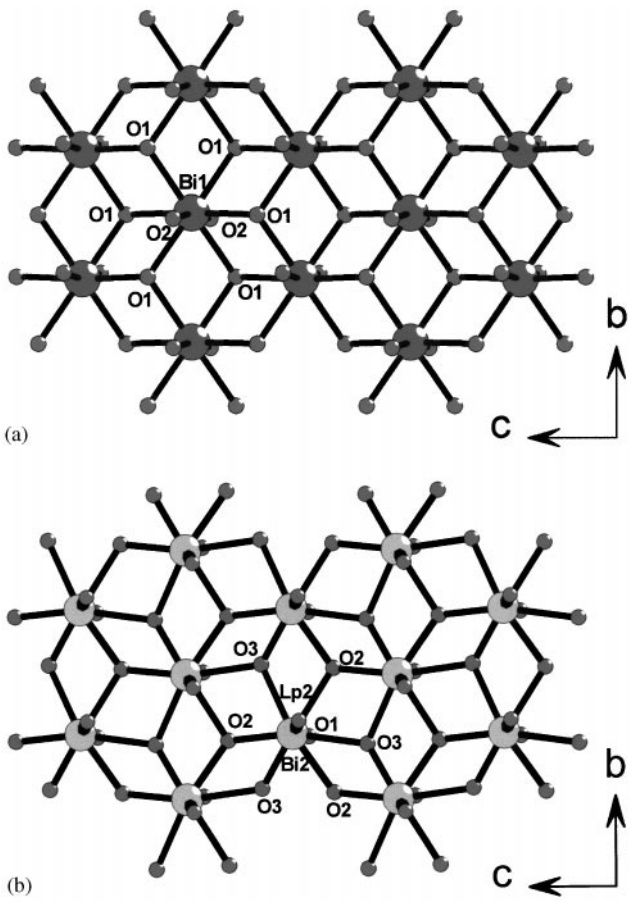


**FIG. 4.** Projections on (100) of the (a) La–$Bi_{(1)}$–O layer, and the (b) $Bi_{(2)}$–O layer.

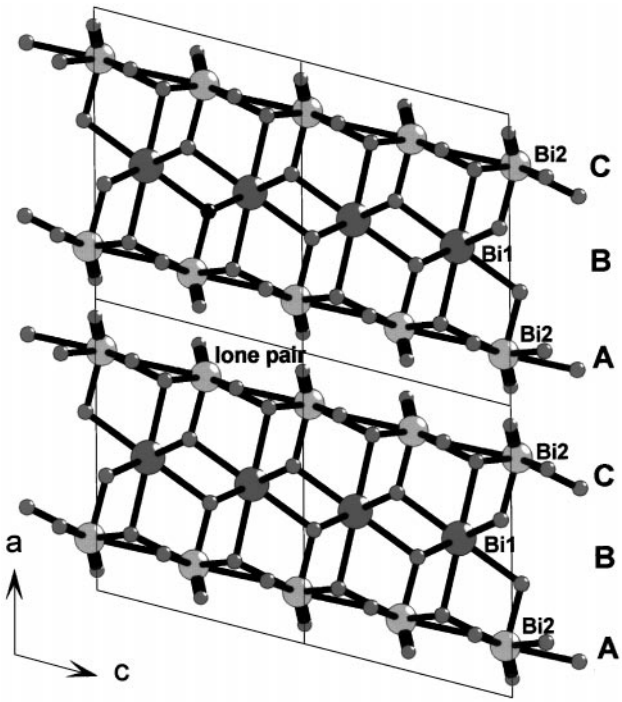


**FIG. 5.** Projection on (010) of six successive Bi–O layers visualizing the ABC sequence of the layer piling and the orientations of the $Bi_{(2)}$ lone-pair electrons.

a very distorted polyhedron, with two very short distances (2.05 and 2.09 Å for respectively the $O_{(3)}$ and $O_{(1)}$ atoms) and five normal distances varying from 2.31 to 2.49 Å. This distorted environment is often observed when a Bi atom possesses a lone pair and the refinement of the $Bi_{(2)}$ electronic lone pair Lp2 places it 1.22 Å from the nucleus, to occupy the interlayer between adjacent $Bi_{(2)}$–O layers (see Table 5).

Each La–$Bi_{(1)}$ atom shares $O_{(1)}$ atoms with the six neighboring cations La–$Bi_{(1)}$ to form a mixed (La–Bi)–O layer parallel to the plan (*b*, *c*), Fig. 4a. In the same manner, each $Bi_{(2)}$ atom shares also oxygen atoms with the six closest bismuth atoms, to form a layer parallel to the precedent (Fig. 4b). Thus, the crystal structure can be described by a piling of layers *ABC*, *ABC*, etc., in the *a*-axis direction, where layers *A* and *C* are formed by $Bi_{(2)}$ atoms and their oxygen environment, and layer *B* is constituted by mixed sites La–$Bi_{(1)}$ and their oxygen atoms (Fig. 5). The cohesion between layers *A* and *B* is ensured by the $O_{(1)}$ and $O_{(2)}$ atoms with long distances to the La–$Bi_{(1)}$ atoms (Fig. 3).

### *ε-Solid Solution Characterization*

For samples initially quenched in liquid nitrogen and then annealed at 300°C for 60 h, the complete transformation of the *β*-Bi–Sr–O phase into the ε-$Bi_{0.81}La_{0.19}O_{1.5}$-related phase was proved in the wide solid solution domain $0.15 \leq x \leq 0.325$. All X-ray diffraction reflections were indexed on the basis of the monoclinic cell identified during the structural investigation. The parameters were refined using a least-squares method. A breaking point, is observed for $x = 0.175$, essentially for the *a* parameter and the cell volume evolution (Fig. 6). It likely corresponds to the particular composition $Bi_5LaO_9$ ($x = 0.166$) in which the mixed cationic site, evidenced from the structural investigation, is occupied by identical numbers of bismuth and lanthanum atoms.

Complementary to the qualitative Guinier Lenné study of $Bi_{0.81}La_{0.19}O_{1.5}$ previously presented (15), an X-ray thermodiffractometry investigation of this sample has been realized using a Siemens D5000 diffractometer in order to determine the evolution of the cell parameters. The X-ray diagrams were recorded at 27°C and from 50 to 750°C (step

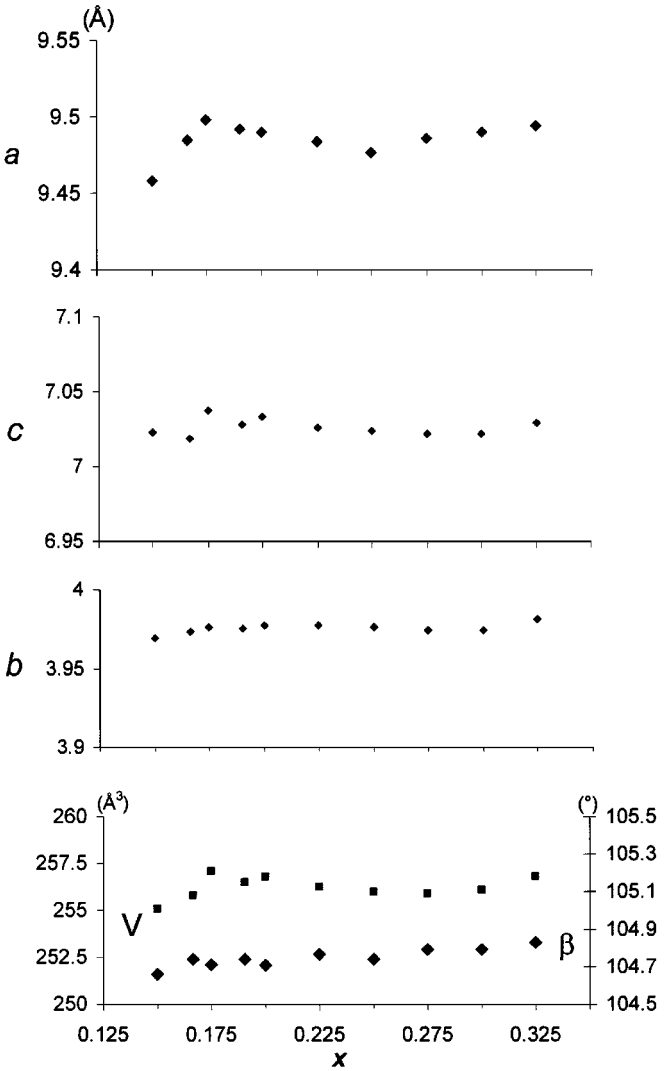


**FIG. 6.** Composition dependence of cell parameters, volume, and *β* angle for the ε-monoclinic phase obtained by annealing at 300°C.

**TABLE 6**
**X-ray Diffraction Data versus Temperature for $Bi_{4.86}La_{1.14}O_9$**

| | Temp. (°C) | *a* (Å) | *b* (Å) | *c* (Å) | *β* (°) |
|---|---|---|---|---|---|
| Hexagonal | 27 | 4.021 | | 27.766 | |
| | 50 | 4.022 | | 27.761 | |
| | 75 | 4.026 | | 27.760 | |
| | 100 | 4.026 | | 27.752 | |
| | 125 | 4.025 | | 27.746 | |
| | 150 | 4.029 | | 27.741 | |
| | 175 | 4.033 | | 27.737 | |
| Monoclinic | 200 | 9.483 | 3.946 | 6.998 | 104.11 |
| | 225 | 9.480 | 3.947 | 7.003 | 104.15 |
| | 250 | 9.485 | 3.951 | 7.009 | 104.14 |
| | 275 | 9.484 | 3.955 | 7.008 | 104.15 |
| | 300 | 9.489 | 3.955 | 7.011 | 104.15 |
| | 325 | 9.491 | 3.957 | 7.015 | 104.17 |
| | 350 | 9.496 | 3.958 | 7.019 | 104.18 |
| | 375 | 9.502 | 3.961 | 7.019 | 104.14 |
| | 400 | 9.506 | 3.963 | 7.025 | 104.13 |
| | 425 | 9.506 | 3.962 | 7.021 | 104.15 |
| | 450 | 9.521 | 3.971 | 7.031 | 104.17 |
| Hexagonal | 475 | 4.051 | | 27.785 | |
| | 500 | 4.053 | | 27.815 | |
| | 525 | 4.056 | | 27.830 | |
| | 550 | 4.058 | | 27.834 | |
| | 575 | 4.058 | | 27.847 | |
| | 600 | 4.062 | | 27.862 | |
| | 625 | 4.063 | | 27.878 | |
| | 650 | 4.064 | | 27.891 | |
| | 675 | 4.065 | | 27.894 | |
| | 700 | 4.079 | | 27.972 | |
| | 725 | 4.080 | | 27.975 | |
| | 750 | 4.080 | | 27.981 | |
| | 775 | 4.081 | | 27.998 | |
| | 800 | 4.084 | | 28.022 | |

25°C) during isothermal treatments, and in each case, the lattice constants were refined from the same series of 21 reflections, using a least-squares method. The obtained values are displayed in Table 6, and the formula unit volume evolution versus temperature is reported in Fig. 7a. Four linear domains characterize successively the phases quenched-$\beta_1$, $\varepsilon$, $\beta_2$, $\beta_1$ with suddenly a drop and two jumps in the volumes. The thermal expansion coefficients determined from the slopes of these domains are $2.78 \times 10^{-5}$, $5.25 \times 10^{-5}$, $5.37 \times 10^{-5}$, and $3.90 \times 10^{-5}$ °$C^{-1}$ respectively. The $\varepsilon$ and $\beta_2$ forms, which exhibit similar coefficients, are evidently discerned because the sudden increase of the formula unit volume at the temperature of the $\varepsilon \rightarrow \beta_2$ transition ($\cong$ 460°C). The discernment of quenched-$\beta_1$ from $\beta_2$ and/or $\beta_1$ appears less evident. Using the data listed in Table 6, the lattice constants thermal expansion coefficients were evaluated. Although quenched-$\beta_1$ and $\beta_2$ present similar *a* coefficients ($\cong 1.74 \times 10^{-5}$°$C^{-1}$), they are distinguished from the corresponding *c* coefficients, respectively $-0.72 \times 10^{-5}$ and $+1.81 \times 10^{-5}$°$C^{-1}$. The thermal expansion coefficients of the *a* and *c* parameters, which make it possible also to characterize unambiguously $\beta_1$ ($0.99 \times 10^{-5}$ and $1.08 \times 10^{5}$°$C^{-1}$), are in a similar ratio to those observed for $\beta_2$.

Figure 7b presents, for a pellet of $Bi_{0.81}La_{0.19}O_{1.5}$, the variation of the thickness (initial value: 4.38 mm) versus the temperature. It is interesting to note the similar evolutions of the thickness and the formula unit volume.

Two series of conductivity measurements have been realized in a wide temperature range with, in both cases, a 20°C step. A series of samples was investigated during a heating–cooling run in the temperature range 100–760°C; another series of measurements was done with cycles in the temperature ranges of the different transformations quenched-$\beta_1 \rightarrow \varepsilon$, $\varepsilon \rightarrow \beta_2$, and $\beta_2 \rightarrow \beta_1$.

Figure 8 presents, as $\log \sigma = f(10^3/T)$ Arrhenius plots, the results obtained for $Bi_{0.81}La_{0.19}O_{1.5}$ using the second thermal program. The three successive heating cooling parts of the thermal treatment, respectively the first $100 \rightarrow 380 \rightarrow 200$°C (8a), the second $200 \rightarrow 500 \rightarrow 300$°C (8b), and the third $300 \rightarrow 800 \rightarrow 300$°C (8c), exhibit distinct linear domains characterizing the quenched-$\beta_1$, $\varepsilon$, $\beta_2$, and $\beta_1$ phases. The irreversibility of the transformations quenched-$\beta_1 \rightarrow \varepsilon$ and $\varepsilon \rightarrow \beta_2$ is here clearly verified. These transformations are marked respectively by a drop and a jump of about one decade of conductivity. The $\beta_2 \rightarrow \beta_1$ transition, evidenced by its well-known jump of $\sigma$, appears quite reversible; the sudden modification of conductivity is only about half a decade. The activation energies for quenched-$\beta_1$, $\varepsilon$, $\beta_2$ and $\beta_1$ are about 0.94, 0.83, 0.84, and 0.21 eV, respectively.

An analogous behavior has been observed for the different samples that were studied in the composition range

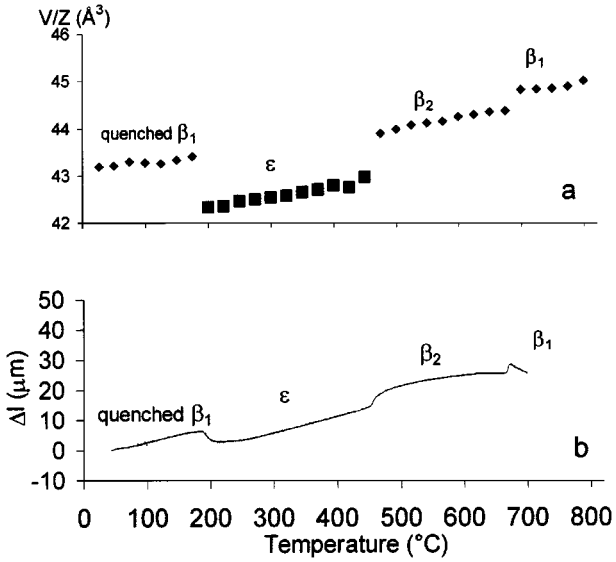


**FIG. 7.** Temperature dependence of (a) unit formula volume and (b) pellet thickness for $Bi_{0.81}La_{0.19}O_{1.5}$ quenched into liquid nitrogen from $\beta_1$ domain.

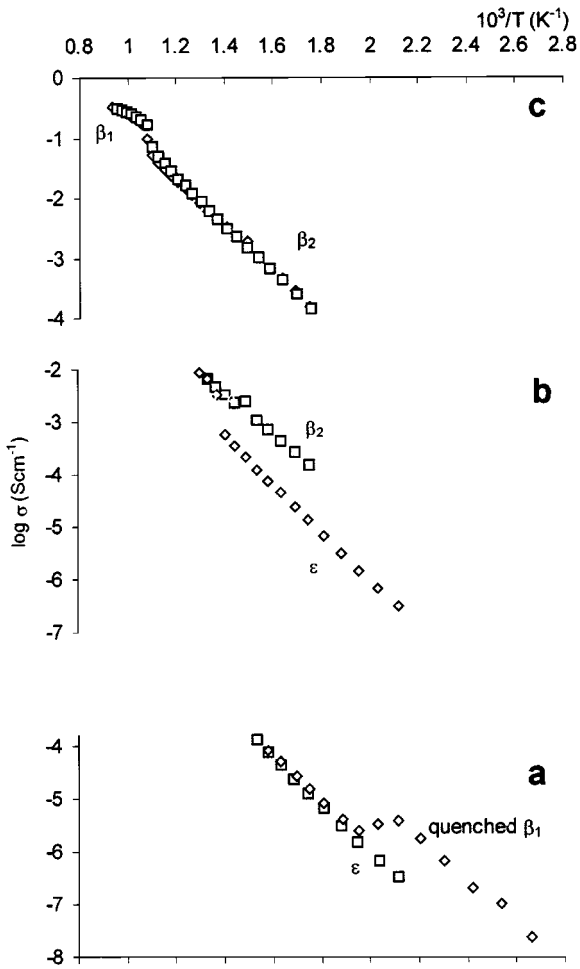


**FIG. 8.** Arrhenius plots (◇, heating; □, cooling) for successive thermal cycles (a, b, c) of the $Bi_{0.81}La_{0.19}O_{1.5}$ pellet quenched into liquid nitrogen from the $\beta_1$ domain.

$0.15 \leq x \leq 0.275$ and no evident correlation between conductivity level or activation energy and $x$ value was revealed. Only an evolution of activation energy of $\varepsilon$ from 0.81 to 1 eV could be noted, when $x$ increases from 0.15 to 0.275.

The Arrhenius plots for samples with $x = 0.3$ and $x = 0.325$ have revealed, in the contrast during the last cooling treatment, besides the $\beta_1 \rightarrow \beta_2$ transition characterized by a drop of conductivity near 600°C, a second drop of $\sigma$ observed at about 320 and 510°C, respectively, followed by a linear Arrhenius domain. Each of these low-temperature domains corresponds to a mixture of the phases $\beta_2$ and $\varepsilon$, which were characterized from the X-ray pattern of ground pellets after the conductivity measurements. Figure 9, on which, besides the plot of the sample $x = 0.3$, the plot for $x = 0.275$ is presented, clearly evidences the new behavior of the samples for $x > 0.275$. When the $\varepsilon$ monoclinic phase is obtained pure from quenched-$\beta_1$ upon either a slow dynamic heating run or an isothermal treatment at about 300°C, it coexists with the $\beta_2$ phase for samples slowly cooled from $\beta_1$. Due to the presence of $\beta_2$ as well as $\varepsilon$, the conductivity of the materials is higher than that of $\varepsilon$ observed during the initial heating for the same temperature range. This interpretation has been confirmed from a Guinier Lenné pattern for the sample with $x = 0.3$, recorded during an heating–cooling cycle between 100 and 720°C.

All samples of the quenched-$\beta_1$ variety have been investigated using DTA in order to determine the transition temperatures $\varepsilon \rightarrow \beta_2$ and $\beta_2 \rightarrow \beta_1$. All DTA curves were similar to the thermogram presented recently for the $Bi_{0.81}La_{0.19}O_{1.5}$ material (15). After a broad exothermal effect corresponding to the formation of the $\varepsilon$ phase, two endothermal peaks relative to $\varepsilon \rightarrow \beta_2$ and $\beta_2 \rightarrow \beta_1$ were evidenced. The transition temperatures were in agreement with the temperatures corresponding to conductivity jumps in the log $\sigma = f(10^3/T)$ Arrhenius plots. Taking into account the fact that it is impossible to obtain identical cooling conditions for a series of samples that are quenched (from the $\beta_1$ domain) for a wide composition range, the purity of quenched-$\beta_1$ and then of $\varepsilon$ cannot be confirmed therefore, the composition dependence of the thermal peaks intensity has not been interpreted. Figure 10 proposes the temperature–composition domains of the different phases of

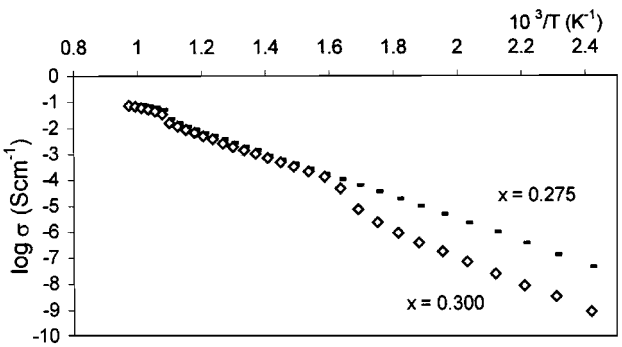


**FIG. 9.** Arrhenius plots upon cooling runs for the $Bi_{1-x}La_xO_{1.5}$ samples ($x = 0.275$, 0.3).

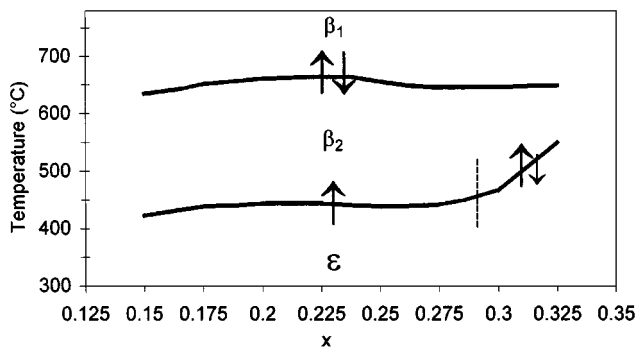


**FIG. 10.** Composition dependence of transition temperatures between phases $\varepsilon$, $\beta_2$, and $\beta_1$ for $Bi_{1-x}La_xO_{1.5}$ solid solution.

the $Bi_{1-x}La_xO_{1.5}$ system obtained from the pure monoclinic phase.

## ACKNOWLEDGMENT

The authors are very grateful to Mrs. Nora Djelal in her help in samples syntheses and realization of conductivity and dilatometry measurements.

## REFERENCES

1. M. Drache, S. Obbade, J. P. Wignacourt, and P. Conflant, *J. Solid State Chem.* **142,** 349 (1999).
2. P. Conflant, J. C. Boivin, G. Nowogrocki, and D. Thomas, *Solid State Ionics* **9/10,** 925 (1983).
3. P. Conflant, J. C. Boivin, and D. Thomas, *J. Solid State Chem.* **35,** 192 (1980).
4. P. Conflant, Thesis, University of Lille, 1985.
5. M. Drache, J. P. Wignacourt, and P. Conflant, *Solid State Ionics* **86–88,** 289 (1996).
6. D. Mercurio, M. El Farissi, J. C. Champarneaud-Mesjard, B. Frit, and P. Conflant, *J. Solid State Chem.* **80,** 133 (1989).
7. D. Mercurio, J. C. Champarneaud-Mesjard, B. Frit, P. Conflant, J. C. Boivin, and T. Vogt, *J. Solid State Chem.* **112,** 1 (1994).
8. S. K. Blower and C. Greaves, *Mater. Res. Bull.* **23,** 765 (1988).
9. R. J. D. Tilley, *J. Solid State Chem.* **41,** 233 (1982).
10. R. L. Withers and H. Rossell, *J. Solid State Chem.* **118,** 66 (1995).
11. R. D. Shannon and C. T. Prewitt, *Acta Crystallogr. Sect. B* **26,** 1046 (1970).
12. R. D. Shannon, *Acta Crystallogr. Sect. A* **32,** 751 (1976).
13. P. Conflant, C. Follet-Houttemane, and M. Drache, *J. Mater. Chem.* **1,** 649 (1991).
14. M. Drache, J. P. Wignacourt, and P. Conflant, *J. Solid State Chem.* **149,** 341 (2000).
15. M. Drache, J. P. Wignacourt, and P. Conflant, *J. Solid State Chem.* **151,** 281 (2000).
16. J. Rodrigez Carvajal, M. T. Fernandez Diaz, and J. L. Martinez, *J. Phys. Cond. Mater.* **3,** 3215 (1991).
17. A. Altomare, G. Cascarano, G. Giacovazzo, A. Guagliardi, M. C. Burla, G. Plidori, and M. Camalli, *J. Appl. Crystallogr.* **27,** 435 (1994).
18. A. Altomare, M. C. Burla, G. Cascarano, G. Giacovazzo, A. Guagliardi, A. G. G. Moliterni, and G. Plidori, *J. Appl. Crystallogr.* **28,** 842 (1995).
19. P. E. Werner, L. Erikson, and M. Westdhal, *J. Appl. Crystallogr.* **18,** 367 (1985).
20. H. M. Rietveld, *Acta Crystallogr.* **22,** 151 (1967).
21. H. M. Rietveld, *J. Appl. Crystallogr.* **2,** 65 (1969).
22. C. Caglioti, A. Paoletti, and E. P. Ricci, *Nucl. Instrum. Methods* **3,** 223 (1958).
23. R. D. Shannon, *J. Appl. Phys.* **73**(1), 348 (1993).
24. E. Morin, G. Wallez, S. Jaulmes, J. C. Couturier, and M. Quarton, *J. Solid State Chem.* **137,** 283 (1998).
25. A. Verbaere, R. Marchand, and M. J. Tournoux, *J. Solid State Chem.* **23,** 383 (1978).
26. P. P. Ewald, *Ann. Phys.* **64,** 253 (1921).
27. L. Pauling, "The Nature of the Chemical Bond." Cornell Univ. Press, New York, 1939.
28. A. L. Allred and E. G. Rochow, *J. Inorg. Nucl. Chem.* **5,** 264 (1958).